Chemical Science

Accepted Manuscript

This article can be cited before page numbers have been issued, to do this please use: J. Duan, H. Zhou, W. Bi, J. Liu, L. Xu, W. He, X. Sun, H. Hu, W. Lyu and Y. Liao, *Chem. Sci.*, 2026, DOI: 10.1039/D5SC07537H.

ROYAL SOCIETY OF CHEMISTRY

rsc.li/chemical-science

View Article Online
DOI: 10.1039/D5SC07537H

ARTICLE

Curvature Defect Engineering towards High Performance COF-based Cathode in Lithium-ion Batteries

Received 00th January 20xx,
Accepted 00th January 20xx

DOI: 10.1039/x0xx00000x

Ju Duan[a], Haojie Zhou[a], Wenxiao Bi[a], Jiawei Liu[a], Linchu Xu[a], Weisi He[a], Xinyuan Sun[a], Huawei Hu[a], Wei Lyu*[a], Yaozu Liao*[a]

Covalent organic frameworks (COFs), a type of functional-oriented porous material, show great potential in rechargeable batteries owing to well-defined ions channels and flexible framework design. However, the active sites in COFs are almost impossible to be fully utilized caused by the insufficient electron transport or ions diffusion. Here, a defect-rich COF@CNT cathode (RBT-COF@CNT-50) was designed by curvature defect engineering to enhance electrochemical reaction kinetics. The synergistic effect of the defect-rich D-A framework with CNT interlaced network endows RBT-COF@CNT-50 higher electron conductivity of 2.65×10^{-4} S m^{-1}. More defects emergence with polar functional groups in RBT-COF@CNT caused by the curvature-induced effect contribute to faster ions diffusion. Consequently, RBT-COF@CNT-50 delivers higher reaction rate of 1.49×10^{-6} mol s^{-1} m^{-2}. As excepted, RBT-COF@CNT-50 reveals a high specific capacity of 302 mAh g^{-1} at 0.1 A g^{-1}. It also displays excellent long-term cycling performance with 148 mA g^{-1} at 2 A g^{-1} for continuously 2000 cycles and 124 mA g^{-1} with capacity attenuation rate of 0.004% per cycle at 10 A g^{-1}, outperforming most reported COFs/carbon composites cathodes. This work offers in-depth insights in constructing high performance COF-based cathode by enhancing electrochemical reaction kinetics within a curvature defect engineering.

Introduction

Lithium-ion batteries (LIBs), as an emerging technological innovation, have grown at an astonishing rate throughout society, driving the widespread adoption of renewable energy equipment, including portable electronic devices, electric vehicles, and aerospace applications.[1-3] Nevertheless, the rapidly increasing demand for LIBs presents significant challenges in designing cathode materials to overcome theoretical capacity limitations.[4,5] Different from conventional inorganic cathode materials, organic cathode materials have attracted extensive attention owing to their sustainability, cost-effectiveness, and structural design flexibility.[6-8] Among them, covalent organic frameworks (COFs), crystalline porous materials linked by robust covalent bonds, represent a pioneering material platform that aligns precisely with functional requirements. Their unique features, including well-defined open channels, tunable chemical properties, and large specific surface areas, endow COFs with great potential for energy storage.[8,9] However, optimizing electrochemical reaction kinetics within COFs remains crucial for achieving excellent electrochemical performance.

According to the "*wiring lengths*" concept: $L_e/L_{ions}=(\sigma_e/\sigma_{ions})^{1/2}$, the ions diffusion length (L_{ions}) and electron transfer length (L_e) should be matched to ensure high accessibility of active sites, accompanied by high electron conductivity (σ_e) and ions conductivity (σ_{ions}).[10,11] Therefore, optimizing electrochemical reaction kinetics requires improvements in both electron and ions diffusion. On the one hand, various structural design strategies have been explored to enhance electron transport, including metal ion coordination[12], extended conjugated electron delocalization[13], and donor-acceptor (D-A) mediated electron transport[14]. Particularly, COFs/carbon composites materials has proven to be an effective method, leveraging the excellent electron-donating properties of carbon materials through π-π interactions.[15] On the other hand, although COFs naturally possess well-defined pores that favor ions diffusion, the ions solvation structure inside organic electrode, unlike that in inorganic electrode, still remains a critical factor influencing reaction kinetics.[16] Several approaches have been proposed to regulate solvation structures, such as introducing polar groups[17], modifying framework charges[16], and employing solvent additives[18]. Among these, tailoring the framework polarity is regarded as a convenient and versatile strategy due to the inherent structural diversity of COFs.[17] Nevertheless, achieving simultaneous improvements in electron transport and ions diffusion still proposes significant challenges.

Structural defects, which are inevitably generated during COF synthesis, have been shown strongly influence on electron and ions diffusion.[19,20] Vacancy defects are reported to enhance electron conductivity by introducing additional energy levels around the Fermi level.[19] Notably, vacancy defects may form during COF growth, promoting defects further generation due to the curvature effect of carbon nanotubes (CNTs).[21] In addition, the vacancy defects will endow the framework structure more regulation in the solvation structure, further influencing the ions diffusion.[17] Hence, rationally designing COF carbon composite materials provides an effective

[a] State Key Laboratory of Advanced Fiber Materials, College of Materials Science and Engineering, Donghua University, Shanghai 201620, China.

†Electronic Supplementary Information (ESI) available: details of any supplementary information available should be included here. See DOI: 10.1039/x0xx00000x

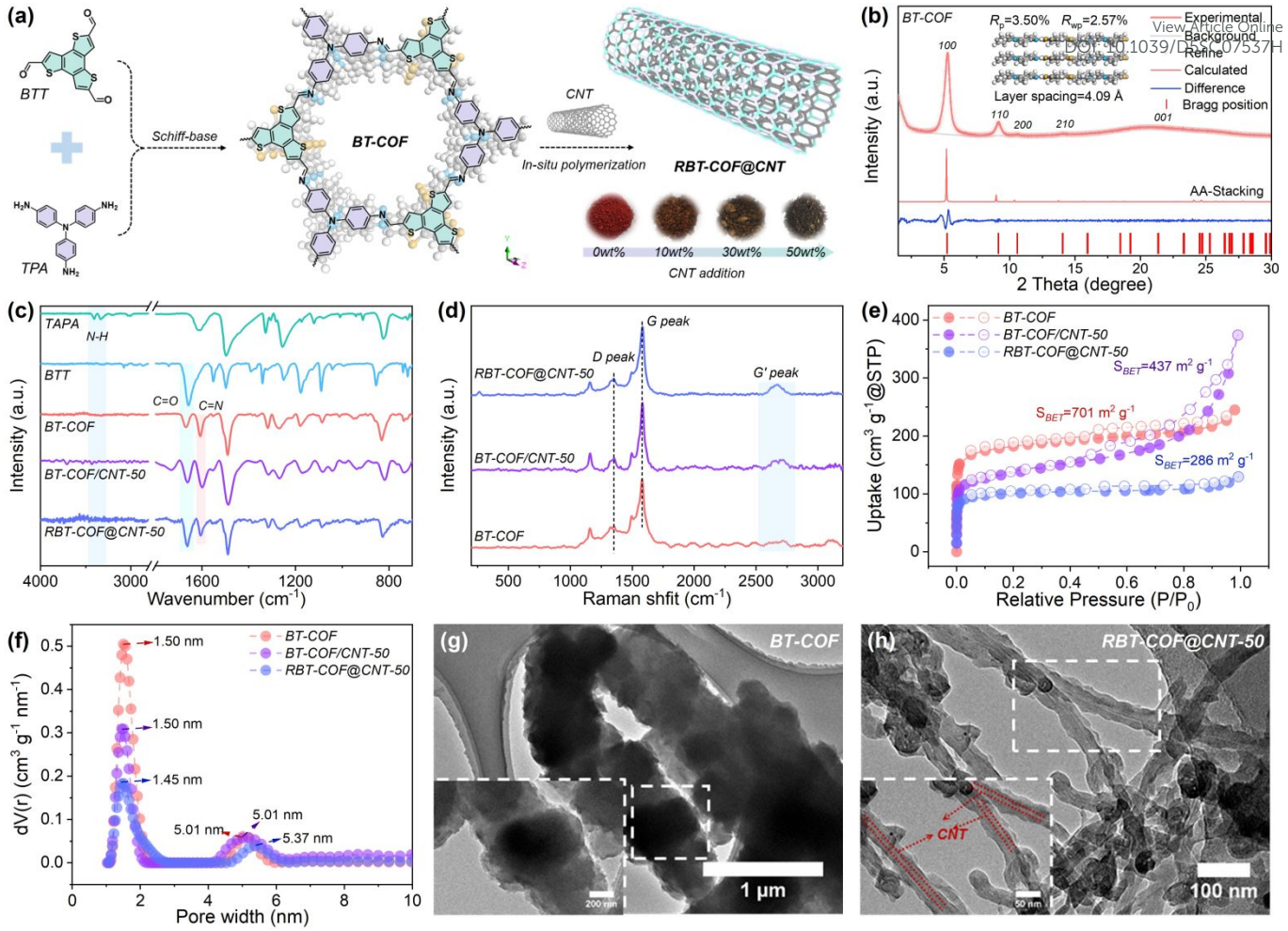

Figure 1. (a) The schematic diagram of BT-COF and RBT-COF@CNT. (b) The PXRD patterns of BTCOF with the AA stacking and Pawley-refined. (c) N_2 isothermal adsorption/desorption curves with (d) pore size distribution and (e) Raman spectra for BT-COF, BT-COF-CNT-50, and RBT-COF@CNT-50. (f) FT-IR spectra of BT-COF and RBT-COF@CNT-50 with the related monomers. TEM images with local selection amplification for (g) BT-COF and (h) RBT-COF@CNT-50.

pathway for achieving high-performance with optimizing electrochemical reaction kinetics.

Herein, we designed a defect-rich COF@CNT cathode material (RBT-COF@CNT-50) with a core-shell structure *via* curvature defect engineering, using CNTs as templates to optimize electrochemical reaction kinetics. The CNTs act as highly conductive cores, providing efficient electron transport pathways, while the covering defect-rich donor–acceptor (D–A) type COF (RBT-COF) shell offers high porosity and abundant active sites. This defect-rich D–A framework on surface of CNTs enables better electron transport with markedly enhancing the electronic conductivity for RBT-COF@CNT-50 (2.65×10^{-4} S m^{-1}) than pristine BT-COF (3.16×10^{-14} S m^{-1}). In addition, more defects promoted by the curvature-induced effect facilitate faster ions diffusion. As a result, RBT-COF@CNT-50 achieves a significantly higher reaction rate (1.49×10^{-6} mol s^{-1} m^{-2}) compared with both BT-COF (0.85×10^{-6} mol s^{-1} m^{-2}) and physical mixing of BT-COF with 50 wt% CNTs (BT-COF/CNT-50, 0.97×10^{-6} mol s^{-1} m^{-2}). As excepted, RBT-COF@CNT-50 reveals a high specific capacity of 302 mAh g^{-1} at 0.1 A g^{-1}, along with better rate performance with 88 mAh g^{-1} even at a high current density of 10 A g^{-1}. It also displays excellent long-term cycling performance at 2 A g^{-1} with 148 mA g^{-1} even after 2000 cycles. When further enhancing to 10 A g^{-1}, RBT-COF@CNT-50 still delivers a high initial discharge specific capacity of 124 mA g^{-1} with capacity attenuation rate of 0.004% per cycle, outperforming most reported COFs/carbon composites cathodes. This work demonstrates a facile yet effective strategy to enhance electrochemical reaction kinetics, offering valuable insights into the development of advanced nanofiber porous cathodes for high-performance energy storage applications.

Results and discussion

In this work, leveraging single-walled carbon nanotubes (CNTs) as structural templates, we engineered a core-shell architecture (denoted as RBT-COF@CNT) through *in-situ* growth with tris(4-aminophenyl)amine motif (TPA, electron donor) as p-type monomers reacted with benzoterthiophene motif (BTT, electron acceptor), promoting optimized electron transport *via* π-π interfacial interactions as shown in **Figure 1a** (see Supporting Information for details).[22] The crystalline structure was validated by the powder X-ray diffraction (PXRD) patterns, revealing an AA stacking mode refined by Pawley fitting using Materials Studio (**Figure 1b** and **Table S1†**). The PXRD pattern of BT-COF closely matches the simulated AA

stacking model, exhibiting low R_p (3.50%) and R_{wp} (2.57%). The ternary structure of TPA imparts BT-COF with a larger interlayer spacing of 4.09 Å. Upon CNT incorporation, the crystallinity is preserved while with reduced diffraction intensity, particularly at 50 wt% CNT loading (RBT-COF@CNT-50, **Figure S1a†**). A distinct peak at ~26.1°, corresponding to the (002) lattice plane of CNTs, is also observed.[23,24]

The chemical structure of RBT-COF was further verified by Fourier-transform infrared spectroscopy (FT-IR, **Figures 1c and S1b†**). The disappearance of N–H stretching (~ 3200–3500 cm^{-1}) from TPA, reduction of the C=O band (1658 cm^{-1}) from BTT, and the appearance of imine (C=N, 1607 cm^{-1}) collectively confirm the formation of BT-COF.[8] Solid-state ^{13}C CP/MAS nuclear magnetic resonance (^{13}C NMR) spectra (**Figure S1c†**) display characteristic peaks of the COF backbone, which broaden upon CNT addition owing to sideband effects arising from the high conductivity of CNTs.[25] Increasing CNT content results in gradually emerging of aldehyde alongside weakened imine bonds, suggesting that CNTs may influence on polymerization and induce additional vacancy defects. X-ray photoelectron spectroscopy (XPS, **Figures S1d† and S1e†**) further supports this result with O 1s spectra, indicating increased defect concentration in RBT-COF formed on CNT surfaces. More framework defects accompanied by gradually increasing CNT proportion can be further verified by electron paramagnetic resonance (EPR) spectra in **Figure S1d†**. One pair of sign peaks located at ~ 3510 G can be observed which represents to the triphenylamine radicals in BT-COF.[26] When the CNTs addition increases to 10 wt%, this characteristic signal peak has improved which maybe owing to enhanced dispersion of COF crystals.[27] Following by the further increasing of CNTs addition proportion to 30% and 50%, the signal peak intensity gradually weakens, suggesting the triphenylamine radicals declines with more framework defects. This phenomenon indicates that the defects will increase accompanied by the CNTs addition enhancement. However, BT-COF/CNT-50 shows no characteristic signal peaks, which is attributed to the electromagnetic shielding effect generated by a high proportion of CNTs with conductive network.[28] Moreover, peak shifts of C=N from 1607 to 1602 cm^{-1} and C=O from 1669 to 1662 cm^{-1} demonstrate strong π-π interfacial interactions between RBT-COF and CNTs. This interaction is also evident in physically mixed between BT-COF and 50wt% CNT (BT-COF/CNT-50).[29,30] Raman spectroscopy reveals distinct G' bands associated with out-of-plane carbon vibrations in CNTs (**Figure 1d**), with intensity progressively increasing from 10 to 50 wt% CNT (**Figure S1f†**). A slight shift in the G band (from 1578 cm^{-1} in BT-COF to 1583 cm^{-1} in BT-COF/CNT-50 and RBT-COF@CNT-50) further evidences π-π interactions between CNTs and BT-COF.[29]

N_2 isothermal adsorption/desorption measurements were conducted to evaluate the *Brunauer-Emmett-Teller* (BET) surface area (S_{BET}) of RBT-COF with different addition content of CNTs in **Figures 1e and S2a†**. Pristine BT-COF exhibits a high S_{BET} of 701 $m^2 g^{-1}$, which decreases to 426, 308, and 286 $m^2 g^{-1}$ with increasing CNT content (10, 30, and 50 wt%, respectively), attributable to the relatively lower surface area of CNTs (334 $m^2 g^{-1}$, **Figure S2b†**). Pore-size distribution, calculated by non-local density functional theory (NLDFT, **Figures 1f and S2c†**), shows that BT-COF possesses a dominant pore size of 1.50 nm, which slightly decreases to 1.45 nm in RBT-COF@CNT-50 due to layer interlacing and stacking disorder (consistent with PXRD in **Figure S1a†**).[31] Notably, the total pore volume significantly decreases, shortening ions diffusion pathway. Additionally, BT-COF displays a mesopore size (5.01 nm) arising from interparticle voids. This mesopore size expands to 5.37 nm in RBT-COF@CNT-50, likely due to improved dispersion of COF nanocrystals by CNTs incorporation. A similar reduction in S_{BET} (437 $m^2 g^{-1}$) and nearly identical pore-size distribution are observed for BT-COF/CNT-50 compared to BT-COF.

Morphological analysis *via* scanning electron microscopy (SEM, **Figure S3a†**) delivers that BT-COF adopts a rod-like morphology composed of aggregated nanocrystals. In contrast, RBT-COF@CNT evolves into a uniform nanofibrous structure with improved COF dispersion as CNTs loading increases (**Figures S3b-S3d†**). Transmission electron microscopy (TEM, **Figures 1g, 1h, and S4†**) further confirms this transformation. Pristine BT-COF forms thick nanocrystalline aggregations (>200 nm), limiting active site accessibility. While, the average thickness of BT-COF shell on the surface of CNTs becomes relatively decreasing and thinner to ~130, ~80, and ~40 nm, respectively, along with the CNT content increasing to 10 wt%, 30 wt%, and 50 wt%, enabling higher surface active sites exposure and shortened ion-diffusion distances.[32] The reduction domain sizes for COF with increasing CNT proportion maybe owing to more heterogeneous nucleation sites based on the strong π–π interaction between COF and CNTs.[15] Elemental mapping based on energy-dispersive X-ray spectroscopy (EDS, **Figure S5†**) indicates homogeneous distribution of C, N, S, and O across the CNT surface. Thermogravimetric analysis (TGA, **Figure S6†**) verifies the RBT-COF content in RBT-COF@CNT-50 (~56%), consistent with the theoretical composition and confirming material accuracy.

To gain deeper insights into the influence of CNTs on the polymerization of BT-COF, density functional theory (DFT) calculations were performed at the B3LYP/6-31G(d) level. Upon CNTs introduction, the spatial configuration of BT-COF changes from a planar to a curved surface due to substrate curvature effects (**Figure 2a**). The formation of the unique core-shell architecture in BT-COF@CNT is primarily attributed to π-π interactions between the BT-COF framework and CNTs, as indicated by independent gradient model based on Hirshfeld partition (IGMH) analysis (**Figure 2a**).[24,33] This curvature-induced configuration disrupts framework stacking, thereby generating additional defects in the RBT-COF shell as CNT loading increases. Importantly, the strong π-π interaction also facilitates electron transport by coupling with the intrinsic high electron conductivity of CNTs.[32]

The defect-rich nature of the BT-COF shell was further evaluated by molecular electrostatic potential (MESP) mapping (**Figure 2b**). By comparison, the formyl group exhibits a lower electrostatic potential (-1.58 eV) than the imine group (-1.09 eV), suggesting that defects in RBT-COF more readily coordinate cations from the electrolyte. Moreover, the average MESP value of RBT-COF (-0.21 kcal mol^{-1}) is higher than that of BT-COF (-0.46 kcal mol^{-1}), owing to the loss of one electron-donating TPA unit. More electron-deficient characteristics of RBT-COF enhances anions interaction from the electrolyte.[16] The improved electron transport properties of RBT-COF are further supported by the highest occupied molecular orbital-lowest unoccupied molecular orbital (HOMO-LUMO) energy level with energy gap (ΔE_g, **Figures 2c and 2d**). The RBT-COF framework exhibits a narrower HOMO-LUMO gap (2.77 eV) compared with

View Article Online
DOI: 10.1039/D5SC07537H

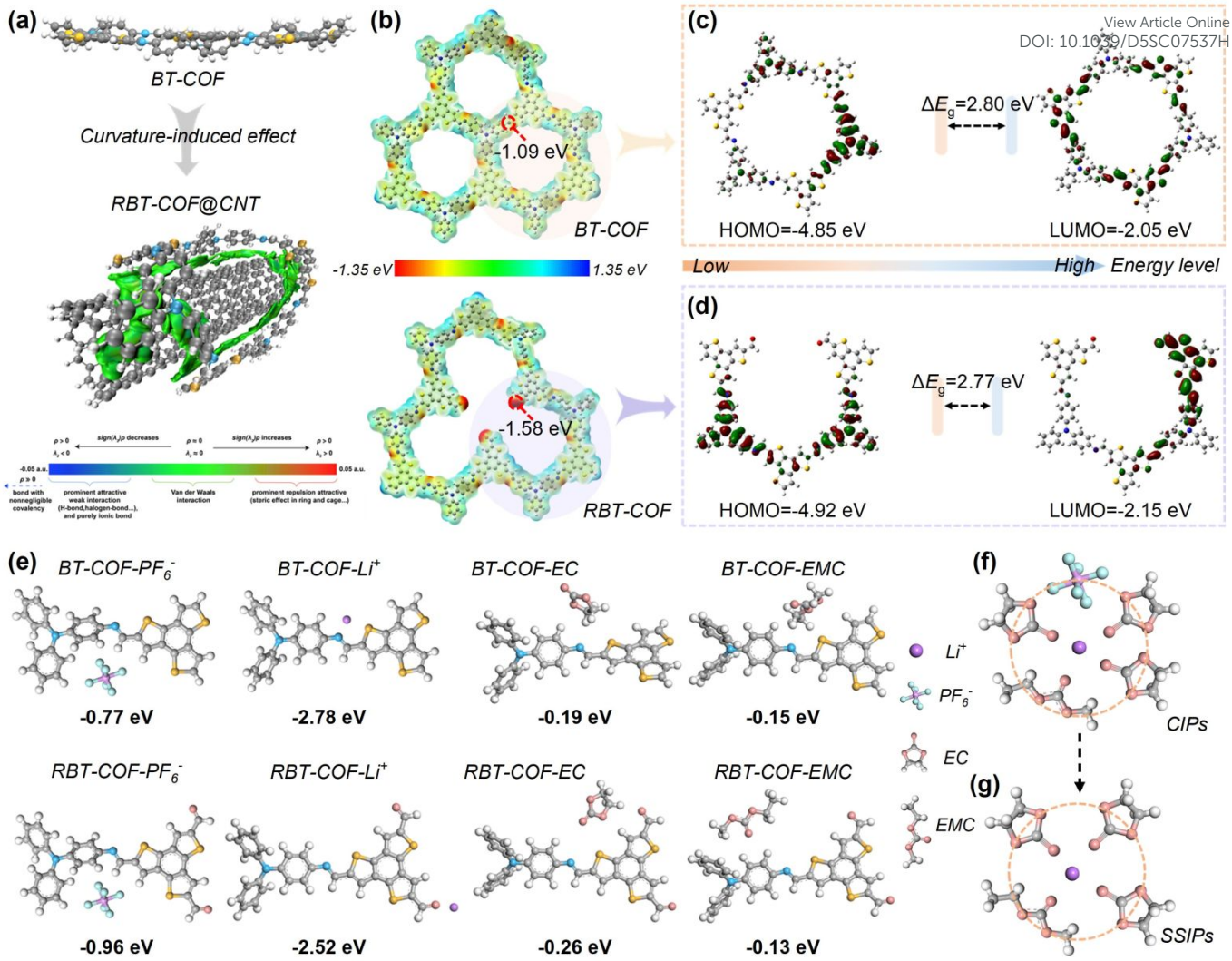

Figure 2. (a) The structural change representation from BT-COF to RBT-COF@CNT and weak interaction regions visualized with a δ_g^{inter} isovalue of 0.005 a.u. in the IGMH analysis for RBT-COF@CNT. (b) MESP of BT-COF and RBT-COF. The HOMO-LUMO energy level with energy gap of the structural units for (c) BT-COF and (d) RBT-COF. (e) The binding energy of BT-COF and RBT-COF with different electrolyte composition. The solvation structure in (f) BT-COF and (g) RBT-COF.

BT-COF (2.80 eV), arising from a reduced LUMO energy from -2.15 to -2.05 eV. The HOMO and LUMO levels are evenly distributed on TPA (donor) and BTT (acceptor) units, establishing an efficient D-A electron transport pathway. This arrangement facilitates electron transport from TPA to BTT and simultaneously enhances ions-framework interaction, thereby improving active sites accessibility.[16] In a word, DFT calculations confirm that the unique core-shell RBT-COF@CNT-50 architecture provides dual benefits in enhancing electron transport and defect-inducing active sites formation.

The better electron transport ability of RBT-COF@CNT-50 was further experimentally validated. UV-Vis diffuse reflectance spectra (DRS, **Figure S7a†**) were used to calculate optical energy gaps (**Figure S7b†**). RBT-COF@CNT-50 exhibits a narrower energy gap (1.63 eV) compared to BT-COF (1.92 eV) and BT-COF/CNT-50 (1.79 eV), consistent with enhanced electron transport. Furthermore, the electron conductivity (σ_e) of RBT-COF@CNT-50 reaches 2.65×10^{-4} S m^{-1} (**Figure S8a†**), markedly higher than that of BT-COF (3.16×10^{-14} S m^{-1}) and comparable to that of BT-COF/CNT-50 (8.04×10^{-4} S m^{-1}, **Figure S8b†**) based on **Eq. S1**. These results, in agreement with theoretical predictions, highlight the promoted electron transport by defects effect for RBT-COF and π-π interactions with CNTs.

Unlike inorganic electrode materials, ions diffusion in organic frameworks is strongly influenced by solvation structures.[34] The electron density change of framework can affect the solvation structure stored inside the COF, promoting its transport and dissociation.[35] Defects within the framework play a critical role in regulating these ions diffusion structures, as revealed by binding energy calculations between COFs and electrolyte components (**Figure 2e**). RBT-COF shows stronger binding in TPA with PF_6^- (-0.96 eV) and BTT with EC (-0.26 eV) compared with those in BT-COF (-0.77 and -0.19 eV, respectively), reflecting its more electron-deficient characteristics. This stronger anions-framework interaction promotes a transformation in solvation structures from predominantly contact ion pairs (CIPs, **Figure 2f**) toward solvent-separated ion pairs (SSIPs, **Figure 2g**), thereby accelerating ions diffusion within RBT-COF.[16,36] Raman spectroscopy further confirms this transformation in **Figure S9†**. The proportion of coordinated PF_6^- decreases from 63% to 55%, accompanied by a rise in free PF_6^-,

View Article Online
DOI: 10.1039/D5SC07537H

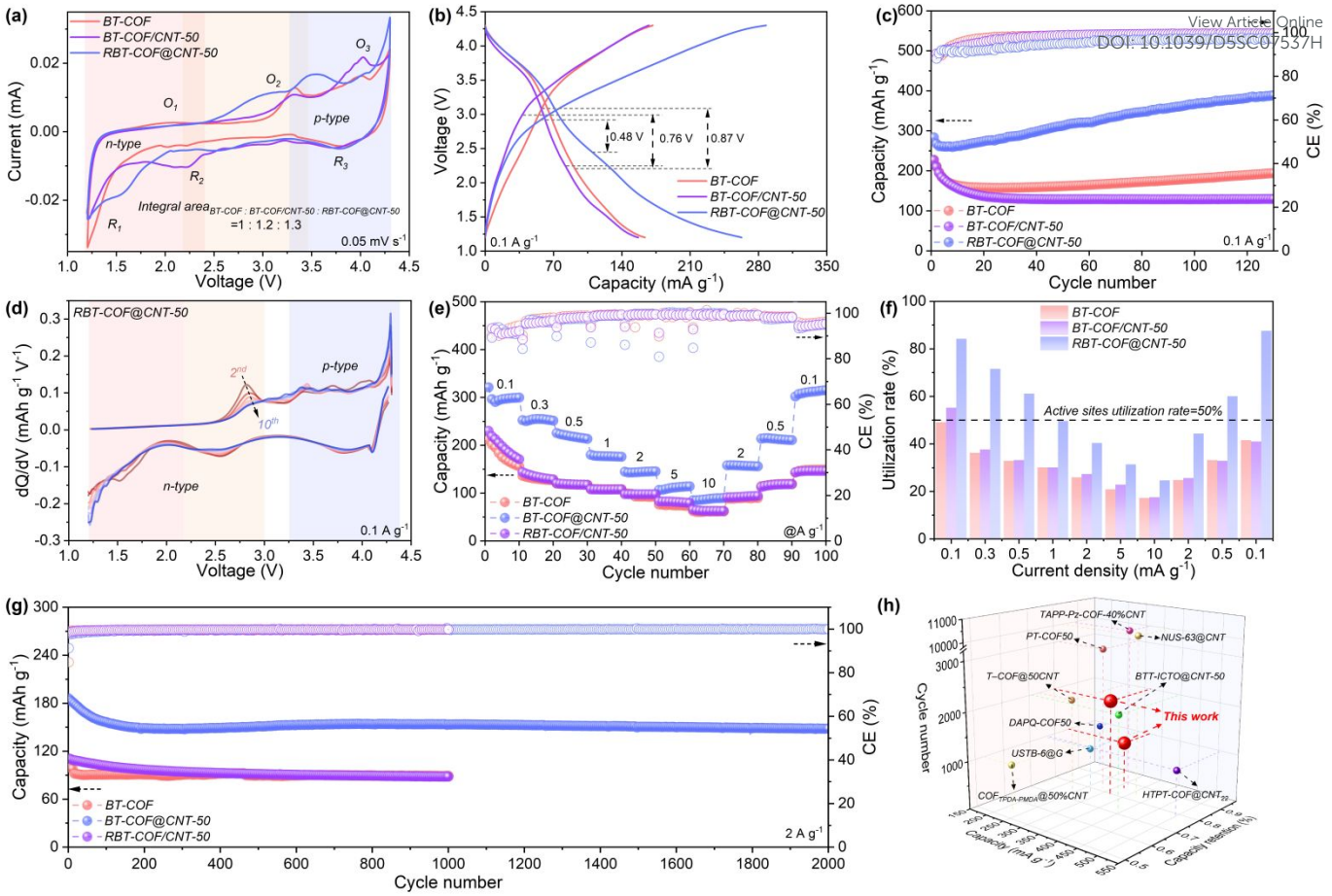

Figure 3. (a) CV curves at 0.05 mV s^{-1}, (b) charging and discharging curves, and (c) cycle performance at 0.1 A g^{-1} of BT-COF, BT-COF/CNT-50, and RBT-COF@CNT-50. (d) dQ/dV curves of RBT-COF@CNT-50. (e) Rate performance, (f) the active sites utilization rates, and (g) long-term cycling performance at 2 A g^{-1} of BT-COF, BT-COF/CNT-50, and RBT-COF@CNT-50. (h) The comparison of electrochemical performance for RBT-COF@CNT-50 with recently reported COFs/carbon composites cathode materials.

indicating a higher transformation proportion of SSIPs. Such defect-induced solvation regulating enables faster ions diffusion which is expected to show superior electrochemical kinetics of RBT-COF@CNT-50.

To investigate the effect of enhanced electron and ion transport on electrochemical performance, BT-COF, BT-COF/CNT-50, and RBT-COF@CNT-50 were evaluated as cathodes for LIBs within 1.2-4.3 V. The cyclic voltammetry (CV) curve of BT-COF exhibits three pairs of redox peaks at 2.0 (O1)/1.3 V (R1), 3.3 (O2)/2.2 V (R2), and 4.0 (O3)/3.8 V (R3) in **Figure 3a**, which representing cations storage at BTT carbons, cations insertion into imine and formyl groups based on similar redox voltage, and anions storage in TPA and BTT units.[37] In contrast, BT-COF/CNT-50 retains three pairs of redox peaks with narrower voltage gaps at 2.2/1.3 V, 3.3/2.2 V, and 4.0/3.7 V, indicating improved reversibility arising from improved electrical conductivity based on π-π interfacial interactions with CNTs. RBT-COF@CNT-50 also displays three pairs of redox peaks including 2.0 (O1)/1.6 V (R1), 3.0 (O2)/2.5 V (R2), and 4.0 (O3)/3.8 V (R3) (**Figure 3a**). While, three pairs of redox peaks in RBT-COF@CNT-50 shows further narrower voltage gaps, especially in redox peaks (O2/R2) of cations insertion into imine and formyl groups which shows larger peak area. These phenomena indicate that this curvature defect engineering is conducive to promoting ion storage with better reaction activity. The O1 peak is relatively weak because of the sluggish ion-release process occurring within the lower-voltage region, which resembles the intercalation behavior observed in graphene.[16] Moreover, unlike the cations coordinated within the BTT units (O1/R1), cations stored at the imine and unreacted aldehyde experience stronger binding interactions as supported by the ESP analysis in **Figure 2b**. Consequently, Li^+ extraction from these sites requires higher redox voltage, giving rise to the O2/R2 peaks with more pronounced current responses.[38] The CV curves of RBT-COF@CNT-10 and RBT-COF@CNT-30 were also observed with similar characteristic in **Figure S10†**. The integrated CV area of RBT-COF@CNT-50 is 1.3 and 1.2 times greater than those of BT-COF and BT-COF/CNT-50, respectively, highlighting enhanced redox kinetics and more accessible active sites enabled by curvature defect engineering.[39] The charging and discharging curves at 0.1 A g^{-1} (**Figure 3b**) corroborate the CV results. RBT-COF@CNT-50 exhibits a discharge plateau at 1.4 V, corresponding to Li^+ storage at BTT, and two additional plateaus at ~2.5 and ~3.8 V, associated with Li^+ insertion into imine/formyl groups and PF_6^- release from TPA/BTT, respectively.[16] Notably, the ~2.5 V plateau is unobvious in BT-COF

View Article Online
DOI: 10.1039/D5SC07537H

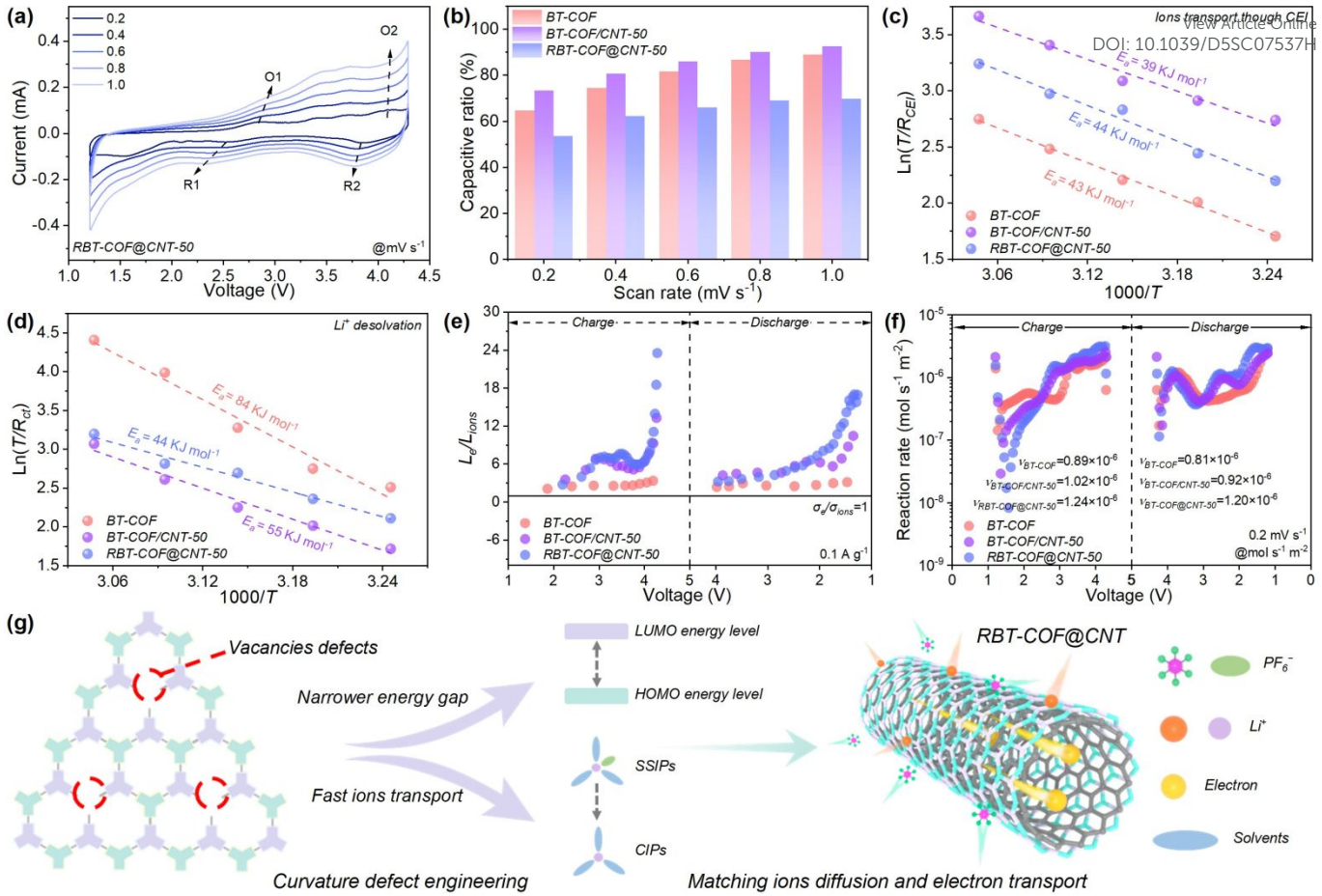

Figure 4. (a) CV curves at various scan rates of RBT-COF@CNT-50. (b) Contribution ratio of the surface-controlled capacitances of BT-COF, BT-COF/CNT-50, and RBT-COF@CNT-50. The diffusion activation energy of (c) Li^+ transport though CEI and (d) Li^+ desolvation for BT-COF, BT-COF/CNT-50, and RBT-COF@CNT-50. (e) The L_e/L_{ions} values and (f) reaction rates of BT-COF, BT-COF/CNT-50, and RBT-COF@CNT-50. (g) The schematic diagram for matching ions diffusion and electron transport by curvature defect engineering.

and BT-COF/CNT-50, underscoring that defects in RBT-COF facilitate the reversible utilization of otherwise less accessible redox sites. Furthermore, the voltage gap significantly reduces from 0.87 V for BT-COF and 0.76 V for BT-COF/CNT-50 to 0.48 V for RBT-COF@CNT-50, indicating suppressed polarization due to curvature defect engineering.

The cycling performance at 0.1 A g^{-1} (**Figure 3c**) demonstrates that RBT-COF@CNT-50 maintains a high specific capacity of 388 mAh g^{-1} after 100 cycles, outperforming BT-COF (195 mAh g^{-1}) and BT-COF/CNT-50 (130 mAh g^{-1}). The initial decrease of capacity can be attributed to the information of cathode electrolyte interphase (CEI).[16] The following activated process may be attributed to the gradually alleviated tightly stacking between the framework.[8] In addition, the first and second-cycle charge/discharge curves of RBT-COF@CNT-50 at 0.1 A g^{-1} was displayed in **Figure S11†**. The initial coulombic efficiencies (CEs) of RBT-COF@CNT-50 are 168% which is attributed to extra lithium ions intercalation during the first discharge process at lower voltage range.[8] The CEs at second-cycle can be reached at 89% which is comparable to commercialized inorganic cathode materials.[40,41] Although the major capacity originates from the n-type region in RBT-COF@CNT-50, design D-A COF with more p-type redox active sites which may be a good solution to increase capacity during high voltage range.[6] The distinct redox peaks can keep well over cycling by differential capacity (dQ/dV) analysis (**Figure 3d**) further evidences stable redox reversibility with high active-site utilization. Rate performance test (**Figure 3e**) reveals the superior kinetics of RBT-COF@CNT-50. At 0.1 A g^{-1}, it delivers 300 mAh g^{-1}, markedly higher than BT-COF (156 mAh g^{-1}) and BT-COF/CNT-50 (171 mAh g^{-1}). Even at elevated current densities of 0.3, 0.5, 1, 2, 5, and 10 A g^{-1}, RBT-COF@CNT-50 still maintains 255, 219, 177, 145, 112, and 88 mAh g^{-1}, respectively, and readily recovers capacities of 158, 214, and 302 mAh g^{-1} when the current densities are returned back to 2, 0.5, and 0.1 A g^{-1}. By comparison, BT-COF and BT-COF/CNT-50 show lower specific capacity at each current density in **Figure 3e**. It should be mentioned that the reason of rapidly capacity decays with increasing current density in RBT-COF@CNT-50 is owing to exacerbating concentration polarization.[42,43] Active sites utilization rates (**Figure 3f**) further highlight the advantage of RBT-COF@CNT-50 with 88% of theoretical capacity calculated by **Eq. S2†** at 0.1 A g^{-1}, while BT-COF and BT-COF/CNT-50 exhibit only 49% and 55%, respectively. Long-term cycling at 2 A g^{-1} (**Figure 3g**) demonstrates the durability of RBT-COF@CNT-50, which delivers 148 mAh g^{-1} after 2000 cycles, significantly higher than BT-COF (89 mAh g^{-1}) and BT-COF/CNT-50 (88

View Article Online
DOI: 10.1039/D5SC07577H

mAh g^{-1}) after 1000 cycles. Different from the cycle performance at 0.1 A g^{-1}, the capacity of all samples will show a gradual decrease and follow by stabilization caused by the high concentration polarization during high current density.[42,43] Even under an ultrahigh current density of 10 A g^{-1}, RBT-COF@CNT-50 retains a high initial discharge capacity of 124 mAh g^{-1} with an ultralow fading rate of 0.004% per cycle in **Figure S12†**. The electrochemical performance of RBT-COF@CNT-10 and RBT-COF@CNT-30 were also measured in **Figure S13†**. Finally, the comprehensive performance superiority of RBT-COF@CNT-50 surpasses against the reported COFs/carbon composites cathodes[15,22,44-50] in terms of capacity, retention, and cycling stability, which can be attributed to its optimized electron pathways and accelerated ions diffusion for efficient utilization of redox-active sites.

The ions diffusion behavior was further evaluated through electrochemical reaction kinetics. As shown in **Figures 4a and S14†**, CV curves at different scan rates (0.2-1.0 mV s^{-1}) were recorded to investigate the ions storage behaviors. For BT-COF (**Figure S14a†**), the oxidation peak at ~3.3 V gradually disappears at scan rates above 0.6 mV s^{-1}. By contrast, the reversible redox peaks O1 (~3.0 V) and R1 (~2.4 V) remain clearly observable even at 1.0 mV s^{-1} for BT-COF/CNT-50 and RBT-COF@CNT-50 (**Figures S14b† and 4a**), which can be attributed to enhanced active sites accessibility enabled by the superior electron transport of CNTs. A similar trend is also observed for RBT-COF@CNT-10 and RBT-COF@CNT-30 (**Figures S14c† and S14d†**). The fitted *b*-values of O1, O2, R1, and R2 are approximately 0.7 based on **Eq. S3†** in **Figure S15†**, indicating that the charge storage process is predominantly diffusion-controlled.[51] The capacitive contribution was further quantified by separating surface-controlled and diffusion-controlled capacitances using **Eq. S4†** (**Figure 4b**). For BT-COF and BT-COF/CNT-50, the surface-controlled contribution increases from 65% and 73% at 0.2 mV s^{-1} to 89% and 93% at 1.0 mV s^{-1}, respectively. In contrast, RBT-COF@CNT-50 consistently exhibits a higher diffusion-controlled contribution, with pseudocapacitance increasing from 54% to 70% as the scan rate increases. The higher diffusion-controlled contribution may be owing to shortening ions diffusion route based on the CNTs introduction. This demonstrates that curvature defect engineering is conducive to ions diffusion within retaining high intrinsic pseudocapacitance.

The enhanced accessibility of active sites was further examined by activation energy (E_a) analysis based on electrochemical impedance spectroscopy (EIS) at various temperatures (**Figure S16†**). The distribution of relaxation times (DRT) method was employed, along with three regions assigned as τ_1 to τ_5, *i.e.*, τ_1 corresponding to contact resistance, τ_2 and τ_3 on behalf of interfacial resistance, and τ_4 and τ_5 representing charge transfer resistance (**Figure S17† and Table S2†**).[52,53] Notably, both interfacial and charge transfer resistances are significantly reduced for RBT-COF@CNT-50, confirming that the defect engineering facilitate electron transport by introducing electron-withdrawing aldehyde groups based on the

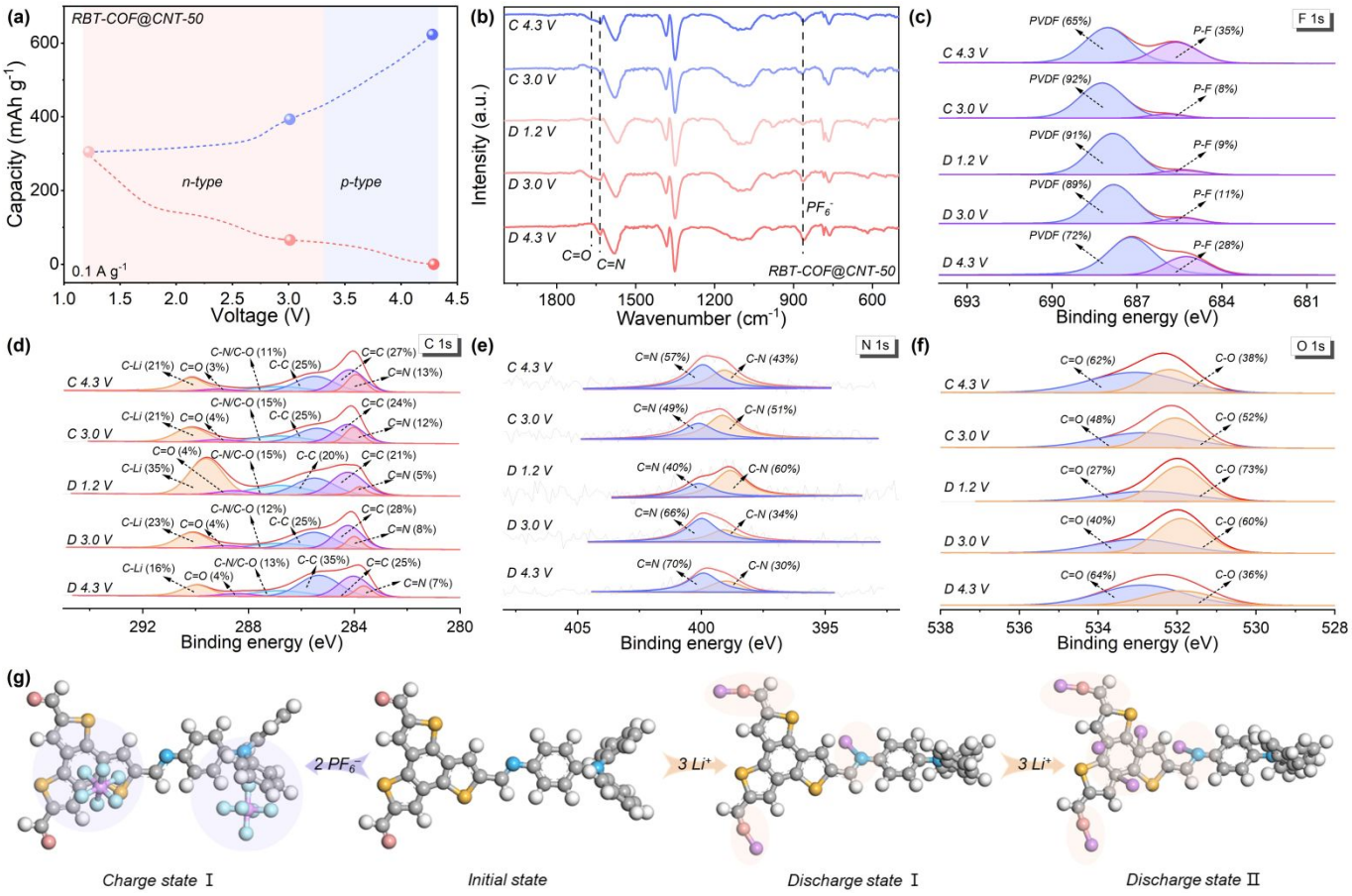

Figure 5. (a) The charge-discharge curve of RBT-COF@CNT-50 electrode at 0.1 A g^{-1} at pristine and selected redox states. (b) The *ex-situ* FT-IR spectra, (c) F 1s, (d) C 1s, (e) N 1s, and (f) O 1s XPS spectra of RBT-COF@CNT-50. (g) DFT calculation of reaction mechanism during bipolar storage process in BT-COF model on the surface of CNT.

View Article Online DOI: 10.1039/D5SC07537H

CNTs conductive network. The E_a was further calculated to distinguish ions transport across CEI in **Figure 4c** and the Li^+ desolvation process in **Figure 4d** based on **Eq. S5†**.[54] The E_a for Li^+ desolvation in RBT-COF@CNT-50 is lowest with 44 kJ mol^{-1} in contrast to BT-COF (84 kJ mol^{-1}) and BT-COF/CNT-50 (55 kJ mol^{-1}), while the E_a for ions transport through the CEI is comparable to that of BT-COF. This result indicates accelerated ions dissociation with higher reaction kinetics in RBT-COF@CNT-50 by curvature defect engineering.

The higher electrochemistry reaction kinetics was further analyzed based on the "*wings length*" concept.[10] The σ_e of the electrode slurries was measured as 0.91×10^{-3}, 2.25×10^{-3}, and 1.37×10^{-3} S m^{-1} for BT-COF, BT-COF/CNT-50, and RBT-COF@CNT-50, respectively in **Figure S18†**. The higher σ_e of RBT-COF@CNT-50 relative to BT-COF is attributed to the synergistic effect of more defects and π-π interactions between CNTs and the COF backbone. Ions conductivity (σ_{ions}) was evaluated using the galvanostatic intermittent titration technique (GITT, **Figure S19†**) based on Fick's law (**Eq. S6†**) and the Nernst–Einstein relation (**Eq. S7†**). Interestingly, the average σ_{ions} of RBT-COF@CNT-50 (0.18×10^{-3} S m^{-1}) is lower than that of BT-COF (1.23×10^{-3} S m^{-1}) and comparable to BT-COF/CNT-50 (0.22×10^{-3} S m^{-1}). The reduced D_{ions} with increasing CNT content likely arises from internal CNT encapsulation during polymerization, which hinders effective ion diffusion. In addition, the low D_{ions} of BT-COF/CNT-50 may also owing to the spatial hindrance effect based on the π-π interactions between CNTs and the COF backbone. Nevertheless, TEM analysis confirms that a thinner COF coating layer forms on CNTs surface with increasing CNT content, thereby shortening ion diffusion pathways and synergistically coupling fast electron transport in RBT-COF@CNT-50.

The calculated L_e/L_{ions} values (**Figure 4e**) show that both BT-COF/CNT-50 and RBT-COF@CNT-50 exceed that of BT-COF at 0.1 A g^{-1}. However, since the electrochemical reactions ultimately rely on active sites within the COF framework, the σ_e of the active material plays a decisive role in determining sites utilization. Indeed, the σ_e of BT-COF is much lower than that of RBT-COF@CNT-50, resulting in limited active site accessibility for BT-COF. This is further confirmed by calculating σ_e/σ_{ions} (**Figure S20†**). Consistently, reaction rate (v) analysis based on Faraday's law (**Eqs. S8–S11†**, **Figure 4f**) shows an enhancement from 0.85×10^{-6} mol s^{-1} m^{-2} (BT-COF) to 0.97×10^{-6} (BT-COF/CNT-50) and 1.22×10^{-6} mol s^{-1} m^{-2} (RBT-COF@CNT-50). To better demonstrate the innovativeness of RBT-COF@CNT-50, the schematic diagram for matching ions diffusion and electron transport by curvature defect engineering is shown in **Figure 4g**. With curvature defect engineering, more vacancies defects emerge with CNTs, which is beneficial to obtain the narrower energy gap and fast ions diffusion for matching ions diffusion and electron transport, achieving better electrochemical reaction kinetics. It should be noted that the gradually decreased S_{BET} with lower pore accessibility (pore volume) can be observed accompanied by increasing the CNTs addition proportion in **Table S3†**. This observation may be attributed to more polymerization site and substrate curvature-induced effect of CNTs for weakening interlayer stacking and generating relative slipping, resulting in worse D_{ions}.[15,24] Therefore, although BT-COF displays higher S_{BET} with better pore accessibility and D_{ions}, the agglomeration morphology of COF nanocrystals still limits the efficient utilization of their active sites.[55]

To gain deeper insights into the charge storage mechanism, *ex-situ* FTIR and XPS measurements were conducted to monitor structural changes of RBT-COF@CNT-50 at selected voltages, based on the proposed bipolarization reaction mechanism with different discharge platforms discussed above (**Figure 5a**). As shown in **Figure 5b**, the stretching vibrations of C=O (1669 cm^{-1}) and C=N (1634 cm^{-1}) progressively weaken as the voltage decreases from 4.3 to 1.2 V during discharging. Upon recharging to 3.0 V, both C=O and C=N peaks reappear, indicating an n-type reaction associated with Li^+ insertion and the formation of C-O-Li and C-N-Li bonds.[16,37] At higher voltages up to 4.3 V, the peak corresponding to PF_6^- (864 cm^{-1}) becomes more pronounced, consistent with a p-type reaction involving anion coordination.[8,16] These observations are corroborated by the F 1s XPS spectra (**Figure 5c**), where the characteristic P-F peak (685 eV) remains dominant at high voltage but gradually decreases upon discharging. The C 1s XPS spectra (**Figure 5d**) further verify the n-type process. The proportion of C-Li (290 eV) increases significantly from 16% to 35% during discharging, partially recovering to 21% upon charging. Concurrently, the proportion of C–N/C–O increases from 13% to 15%, confirming that both C=O and C=N groups serve as redox-active sites during Li^+ insertion. Additional evidence from N 1s and O 1s spectra (**Figures 5e** and 5f) further supports these functional group transformations. Notably, the C=C proportion decreases from 28% to 21%, suggesting that certain C=C bonds within the BTT units also participate in Li^+ binding, contributing to the enhanced capacity.

Based on these observations and supported by DFT calculations, a three-stage charge storage mechanism is proposed in **Figure 5g**. (1) Charge state (p-type reaction): the BTT and TPA units act as active sites for two anions storage above 3.0 V, with a Gibbs free energy (ΔG) of -0.5 eV. (2) Discharge state I (n-type reaction): three Li^+ ions are accommodated in two aldehyde groups and one imine bond of the framework, with ΔG of -4.6 eV. (3) Discharge state II: additional three Li^+ ions are stored at carbon sites of BTT, yielding a lower ΔG of -11.6 eV, validating the proposed binding-site model. All results based on the *ex-situ* spectra analyses and DFT calculations provide compelling evidence that the superior capacity of RBT-COF@CNT-50 originates from its bipolarization-driven charge storage mechanism.

Conclusions

In summary, we propose a defect-rich COF@CNT cathode (RBT-COF@CNT) by curvature defect engineering to optimize electron transport and ions diffusion through a one-pot *Schiff-base* reaction with CNTs as temples. With helpful of multiple electron transport enhancement based on defect-rich D-A system with CNT interlaced network, RBT-COF@CNT achieves excellent electron conductivity of 2.65×10^{-4} S m^{-1}. Benefitted by more polar functional groups originated from defects emergence, RBT-COF@CNT obtain faster ionic atmosphere dissociation and higher reaction rate of 1.49×10^{-6} mol s^{-1} m^{-2}. As excepted, RBT-COF@CNT-50 reveals a high specific capacity of 302 mAh g^{-1} at 0.1 A g^{-1}, good long-term cycling performance with 148 mA g^{-1} at 2 A g^{-1} for continuously 2000 cycles, and high-rate-performance of 124 mA g^{-1} with capacity attenuation rate of 0.004% per cycle at 10 A g^{-1}, outperforming most reported COFs/carbon composites cathodes. This work gives valuable reference for designing porous nanofibers cathode with high

performance by synchronously optimizing electron transport and ions diffusion.

Author Contributions

W. L. and Y.Z. L. conceived the project. J. D., H. J. Z., and X.Y. S. synthesized the samples, performed the structural characterizations, and implement structural simulations. J. D., W.X. B., and J.W. L. participated the electrochemical tests. L.C. X. conducted DFT theoretical calculations. W.S. H. and H.W. H. performed the format of manuscript. All authors analyzed the results and commented on the manuscript.

Conflicts of interest

There are no conflicts of interest to declare.

Data availability

The data supporting this article have been included as part of the ESI.†

Acknowledgements

The authors thank for the financial support from the National Natural Science Foundation of China (52373172, 52073046, and 52473055), the National Key Research and Development Program of China (2022YFB3807100 and 2022YFB3807102), the Key Technology Research and Development Program of Shanghai (25CL2900800), the Chang Jiang Scholar Program (T2023082), the Program of Shanghai Academic Research Leader (21XD1420200), the Natural Science Foundation of Shanghai (23ZR1401100), and the Fundamental Research Funds for the Central Universities (CUSF-DH-D-2025003).

References

1 T. Jiang, D. Shen, Z. Zhang, H. Liu, G. Zhao, Y. Wang, S. Tan, R. Luo, and W. Chen, *Nat. Rev. Clean Technol.*, 2025, ***1***, 474–492.
2 Y. Xu, L. Jiao, J. Ma, P. Zhang, Y. Tang, L. Liu, Y. Liu, H. Ding, J. Sun, M. Wang, Z. Li, H.-L. Jiang, and W.Chen, *Joule*, 2023, ***7***, 515–528.
3 A. Mahmood, Z. Bai, T. Wang, Y. Lei, S. Wang, B. Sun, H. Khan, K. Khan, K. Sun, and G. Wang, *Chem. Soc. Rev.*, 2025, ***54***, 2369–2435.
4 Y. Xu, M. Wang, M. Sajid, Y. Meng, Z. Xie, L. Sun, J. Jin, W. Chen, and S. Zhang, *Angew. Chem. Int. Ed.*, 2024, ***63***, e202315931.
5 M. Zheng, X. Zhu, H. Zheng, Z. Bo, and J. Lu, *Nat. Energy*, 2025, ***10***, 789–792.
6 K. Amin, B. C. Baker, L. Pan, W. Mehmood, Z. Hao, R. Nawaz, Z. Wei, and C. F. J. Faul, *Adv. Mater.*, 2025, ***37***, 2410262.
7 A. L. Waentig, X. Li, M. Zhao, S. Haldar, P. Koko, S. Paasch, A. Mueller, K. M. G. Alvarez, F. Auras, E. Brunner, A. Schneemann, J.-Q. Huang, S. Kaskel, M. Wang, and X. Feng, *Chem. Sci.*, 2025, ***16***, 4152–4158.
8 J. Duan, K. Wang, L. Teng, H. Liu, L. Xu, Q. Huang, Y. Li, M. Liu, H. Hu, X. Chen, J. Wang, W. Yan, W. Lyu, and Y. Liao, *ACS Nano*, 2024, ***18***, 29189.
9 L. Zhu, Y. Cao, T. Xu, H. Yang, L. Wang, L. Dai, F. Pan, C. Chen, and C. Si, *Energy Environ. Sci.*, 2025, ***18***, 5675–5739.
10 C. Zhu, R. E. Usiskin, Y. Yu, and J. Maier, *Science*, 2017, ***358***, eaao2808.
11 J. Zheng, R. Garcia-Mendez, and L. A. Archer, *ACS Nano*, 2021, ***15***, 19014−19025.
12 Y. Li, J. Duan, Y. Wang, L. Teng, H. Liu, J. Li, M. Liu, W. He, H. Hu, L. Wang, W. Lyu, and Y. Liao, *Chem. Sci.*, 2025, ***16***, 11311−11321.
13 X. Xu, S. Zhang, K. Xu, H. Chen, X. Fan, and N. Huang, *J. Am. Chem. Soc.*, 2023, ***145***, 1022–1030.
14 L. Guo, L. Gong, Y. Yang, Z. Huang, X. Liu, and F. Luo, *Angew. Chem. Int. Ed.*, 2025, ***64***, e202414658.
15 L.Yao, C. Ma, L. Sun, D. Zhang, Y. Chen, E. Jin, X. Song, Z Liang, and K.-X. Wang, *J. Am. Chem. Soc.*, 2022, ***144***, 23534–23542.
16 J. Duan, F. Chen, H. Yu, S. Zhu, L. Teng, K. Wang, T. Chen, W. Lyu, H. Hu, and Y. Liao, *Angew. Chem. Int. Ed.*, 2025, ***64***, e202505207.
17 G. Lai, J. Lin, W. Mo, X. Li, X. Jin, M. Wu, and F. Liu, *J. Am. Chem. Soc.*,2025, ***147***, 13071–13081.
18 Z. Jiang, M. Pang, C. Luo, Z. Yao, T. Fu, T. Pan, W. Sun, Y. Li, Q. Guo, S. Xiong, C. Zheng, G. Zhou, S. Liu, *Energy Storage Mater.*, 2024, ***72***, 103729.
19 W. Deng, G. Li, and X. Wang, *Adv. Funct. Mater.*, 2024, ***34***, 2405012.
20 K. Du, L. Xiong, C. Fu, X. Ni, J.-L. Bredas, and H. Li, *ACS Materials Lett.*, 2024, ***6***, 335–344.
21 Z. Guo, H. Wu, Y. Chen, S. Zhu, H. Jiang, S. Song, Y. Ren, Y. Wang, X. Liang, G. He, Y. Li, and Z. Jiang, *Angew. Chem. Int. Ed.*, 2022, ***61***, e202210466.
22 Q. Xu, Z. Liu, Y. Jin, X. Yang, T. Sun, T. Zheng, N. Li, Y. Wang, T. Li, K. Wang, and J. Jiang, *Energy Environ. Sci.*, 2024, ***17***, 5451–5460.
23 J. He, Y. Zhao, Y. Li, Q. Yuan, Y. Wu, K. Wang, K. Sun, J. Wu, J. Jiang, B. Zhang, L. Wang, and M. Fan, *Nano-Micro Lett.*, 2025, ***17***, 221.
24 D. Jiang, R. Xu, L. Bai, J. P. Hill, J. Henzie, L. Zhu, W. Xia, R. Bu, Y. Zhao, Y. Kang, T. Hamada, R. Ma, N. Torad, J. Wang, T. Asahi, X. Xu, and Y. Yamauchi, *Adv. Funct. Mater.*, 2024, ***34***, 2407479.
25 B. A. Atterberry, P. Paluch, A. R. Lamkins, W. Huang, and A. J. Rossini, *J. Am. Chem. Soc.*, 2025, ***147***, 14411–14421.
26 Y. Xie, S. Wu, Z. Zhu, J. Wang, Z. Kuang, L. Zhang, A. Abdurahman, Q. Peng, and X. Ai, *Angew. Chem. Int. Ed.*, 2025, ***64***, e202515346.
27 S. Kang, Y. Jiang, Y. Shi, X. Lou, F. Geng, and B. Hu, *Chem. Mater.*, 2024, ***36***, 4092–4106.
28 J. Liu, Q. Guo, H. Tian, Y. Cheng, X. Xu, Z. Zhang, H. Hao, Z. Ding, K. Jiao, J. Zheng, J. Zhang, and X. Gao, *Matter*, 2025, ***8***, 102427.
29 Y. Zhang, M. Chen, X. He, E. Zhao, H. Liang, J. Shang, K. Liu, J. Chen, S. Zuo, and M. Zhou, *Nat. Commun.*, 2025, ***16***, 2652.
30 Q. Li, D.-D. Ma, W.-B. Wei, S.-G. Han, L. Zheng, and Q.-L. Zhu, *Adv. Energy. Mater.*, 2024, ***14***, 2401314.
31 Z. Lei, Q. Yang, Y. Xu, S. Guo, W. Sun, H. Liu, L.-P. Lv, Y. Zhang, and Y. Wang, *Nat. Commun.*, 2018, ***9***, 576.
32 W. Yuan, J.Weng, M. Ding, H.-M. Jiang, Z. Fan, Z. Zhao, P. Zhang, L.-P. Xu, and P. Zhou, *Energy Storage Mater.*, 2023, ***65***, 103142.
33 Y. Zhuang, H. Yang, Y. Li, Y. Zhao, H. Min, S. Cui, X. Shen, H.-Y. Chen, Y. Wang, and J. Wang, *ACS Nano*, 2025, ***19***, 11058−11074.

View Article Online
DOI: 10.1039/D5SC07537H

34 C. Liu, X. Huang, X. Yu, Z. Wang, Y. Shen, S. Yuan, and Y. Wang, *Angew. Chem. Int. Ed.*, 2025, ***64***, e202415915.
35 D.-H. Guan, X.-X. Wang, L. Li, G.-N. Chen, G.-Y. Qiao, and J.-J. Xu, *J. Am. Chem. Soc.*, 2025, ***147***, 38078–38088.
36 C. Zhou, Y. Zhou, S. Hao, G. Li, S. Liu, and X. Gao, *Cell Rep. Phy. Sci.*, 2024, ***5***, 101999.
37 Q. Bai, J. Huang, K. Tang, Y. Zhu, and D. Wu, *Adv. Mater.*, 2025, ***37***, 2416661.
38 S. Zheng, D. Shi, T. Sun, L. Zhang, W. Zhang, Y. Li, Z. Guo, Z. Tao, and J. Chen, *Angew. Chem. Int. Ed.*, 2023, ***62***, e202217710.
39 J. Duan, W. Wang, D. Zou, J. Liu, N. Li, J. Weng, L.-P. Xu, Y. Guan, Y. Zhang, and P. Zhou, *ACS Appl. Mater. Interfaces*, 2022, ***14***, 31234−31244.
40 Z. Li, Y. Wang, J. Wang, C. Wu, W. Wang, Y. Chen, C. Hu, K. Mo, T. Gao, Y.-S. He, Z. Ren, Y. Zhang, X. Liu, N. Liu, L. Chen, K. Wu, C. Shen, Z.-. Ma, and L. Li, *Nat. Commun.*, 2024, ***15***, 10216.
41 P. Yang, L. Shang, H. Wang, Z. Yan, K. Zhang, Y. Li, J. Chen, *Angew. Chem. Int. Ed.*, 2025, ***64***, e202501539.
42 J. Duan, L. Teng, H. Liu, X. Zhang, H. Yu, Q. Huang, Y. Li, M. Liu, H. Hu, W. Lyu, and Y. Liao, *Angew. Chem. Int. Ed.*, 2025, ***64***, e202517853.
43 C. Song, S. H. Han, Y. Choi, H. R. Shin, M. K. Kim, C. Gong, D. Chen, J.-W. Lee, S. Hong, and N.-S. Choi, *Adv. Mater.*, 2025, ***37***, 2418773.
44 H. Gao, A. R. Neale, Q. Zhu, M. Bahri, X. Wang, H. Yang, Y. Xu, R. Clowes, N. D. Browning, M. A. Little, L. J. Hardwick, and A. I. Coope, *J. Am. Chem. Soc.*, 2022, ***144***, 9434–9442.
45 N. Fu, Y. Liu, K. Kang, X. Tang, S. Zhang, Z. Yang, Y. Wang, P. Jin, Y. Niu, and B. Yang, *Angew. Chem. Int. Ed.*, 2024, ***63***, e202412334.
46 Y. Wang, J. Wang, J. Peng, Y. Jiang, Y. Zhu, and Y. Yang, *ACS Nano*, 2024, ***18***, 23958–23967.
47 W. Li, Q. Huang, H. Shi, W. Gong, L. Zeng, H. Wang, Y. Kuai, Z. Chen, H. Fu, Y. Dong, and C. Zhang, *Adv. Funct. Mater.*, 2024, ***34***, 2310668.
48 C. Jia, A. Duan, C. Liu, W.-Z. Wang, S.-X. Gan, Q.-Y. Qi, Y. Li, X. Huang, and X. Zhao, *Small*, 2023, ***19***, 2300518.
49 S. Biswas, A. Pramanik, A. Dey, S. Chattopadhyay, T. S. Pieshkov, S. Bhattacharyya, P. M. Ajayan, and T. K. Maji, *Small*, 2024, ***20***, 2406173.
50 X. Liu, Y. Jin, H. Wang, X. Yang, P. Zhang, K. Wang, and J. Jiang, *Adv. Mater.*, 2022, ***34***, 2203605.
51 H. Gao, Q. Zhu, A. R. Neale, M. Bahri, X. Wang, H. Yang, L. Liu, R. Clowes, N. D. Browning, R. S. Sprick, Marc A. Little, L. J. Hardwick, and A. I. Cooper, *Adv. Energy Mater.*, 2021, ***11***, 2101880.
52 W. Ma, Y. Guo, J. Sun, C. Zhang, Y. Zhu, H. Sun, L. Huang, Z. Hu, H. Wang, M. Zhu, and G. Wang, *Angew. Chem. Int. Ed.*, 2025, ***64***, e202418999.
53 Y. Lu, C. Z. Zhao, J. Q. Huang, and Q. Zhang, *Joule*, 2022, ***6***, 1172–1198.
54 X. Yin, B. Li, H. Liu, B. Wen, J. Liu, M. Bai, Y. Zhang, Y. Zhao, X. Cui, Y. Su, G. Gao, S. Ding, and W. Yu, *Joule*, 2025, ***9***, 101823.
55 R. Wan, T. Yuan, L. Wang, B. Li, M. Liu, and B. Zhao, *Nat. Catal.*, 2024, ***7***, 1288–1304.

View Article Online
DOI: 10.1039/D5SC07537H

Data Availability Statement

The data supporting this article have been included as part of the ESI.†